Radial fracture during indentation by acute probes: II, Experimental observations of cube-corner and Vickers indentation

DYLAN J. MORRIS[1], AARON M. VODNICK[2] and ROBERT F. COOK[3,4,*]

[1]Center for Materials Research, Washington State University, Pullman, WA 99164-2711, USA
[2]Department of Materials Science and Engineering, Cornell University, Ithaca, NY 14853-1501, USA
[3]Consultant, Minneapolis, MN 55413, USA
[4]Present address: Ceramics Division, National Institute of Standards and Technology, 100 Bureau Drive, Gaithersburg, MD 20899, USA
*Author for correspondence. (E-mail: robert.cook@nist.gov)

Abstract. The companion article proposed a model for radial crack development at sharp contacts. The major extension of this model from previous works is the inclusion of a 'wedging' mechanism, to form a three-stress-field description of indentation crack evolution. Here, the amplitude terms of the three stress-intensity factors comprising the model are calibrated from experimental *in situ* and *post situ* inert-environment radial crack measurements on soda-lime glass. These values are scaled to predict radial crack evolution during cube corner and Vickers indentation of fused silica and soda lime glass in inert and ambient air environments. Both the conventional two-field and the proposed three-field model predictions are compared with radial crack lengths measured during indentation load-unload cycles (through the transparent materials with an *in-situ* apparatus). The three-field model is shown to be a great improvement over the two-field model in the description of crack evolution at cube-corner indentations, particularly with respect to the significant crack extension during loading and the attainment of a maximum crack length during unloading. The three-field model is consistent with observations of Vickers fracture in soda-lime glass and is able to reproduce the features of radial fracture evolution on the 'anomalous' glass, fused silica.

Key words: Acute probe, crack propagation measurements, cube-corner indenter, fused silica, indentation fracture, indentation wedging field, metastable trapped cracks, radial crack, soda-lime glass, Vickers indenter.

1. Introduction

This article evaluates a model developed in the companion work, Part I (Morris and Cook, 2005), for radial crack evolution at elastic-plastic contacts by sharp, acute, rigid indenters. The model is compared with experimental observations of radial crack development for cube-corner and Vickers indentation on soda-lime glass and fused silica during the indentation load-unload cycle. The development of Part I focused on the underlying physics and fracture mechanics of the three component indentation field appropriate for acute probes and demonstrated the qualitative ability of the model to describe radial cracking. Here in Part II, emphasis is placed on *quantitative* assessment of the model, considering both overall agreement between predicted crack length as a function of position in the indentation cycle and specific agreement with the point and relative crack dimension in the indentation unloading

cycle at which cracks attain their maximum length. Particular attention is given to the between-test scaling of calibrated amplitude terms for the three stress-intensity factor components in terms of material properties and indenter acuity.

2. Experimental details

The data used to compare the radial crack evolution models is derived from earlier work–specifically *in-situ* indentation experiments. Such experiments make use of a custom indentation instrument that is capable of recording indentation loads and probe displacements throughout the indentation cycle. This instrument, described elsewhere (Morris and Cook, 2004), may also be mounted upon a metallurgical microscope. With an optically transparent specimen, the development of the contact impression and fracture pattern may be observed through the specimen throughout the entire load-unload cycle. *In-situ* fracture data for cube-corner indentation on soda-lime glass and fused silica are taken from earlier work (Morris and Cook, 2004), while Vickers fracture data on the same materials is unique to this article.

Indentation deformation behavior as a function of indenter acuity was examined using 200 mN peak-load indentations on soda-lime glass generated with a NanoIndenter XP (MTS Corporation, Eden Prairie, Minnesota). Four three-sided diamond pyramids, varying in acuity from the Berkovich to the cube-corner were used. A complete description of these indenter geometries is given in previous work (Morris et al., 2004). The residual impressions were sputter-coated with 50Å of platinum and imaged in a JEOL 6500 field-emission gun scanning-electron microscope (JEOL-USA Inc., Peabody, Massachusetts).

3. Comparison of the indentation wedging model with experiment

3.1. STRESS-INTENSITY FACTORS

The main results and equations from Part I are summarized here for reference. The residual stress intensity factor (SIF), K^R, on radial cracks from a geometrically similar indentation is

$$K^R = \chi^R \frac{P}{c^{3/2}}, \tag{1}$$

where P is the indentation load and c is the radial crack length, defined as the projected length of the surface trace of the crack measured from the indentation center. The magnitude of K^R is fixed by the maximum load, P_{max}, during the unloading half-cycle due to the cessation of plastic deformation after peak load. χ^R is a semi-empirical stress-field amplitude,

$$\chi^R = \xi^R \left(\frac{E}{H} \right)^{1/2} = \zeta^R \left(\cot \phi \right)^{2/3} \left(\frac{E}{H} \right)^{1/2}, \tag{2}$$

where E is the material elastic modulus, H is the hardness, 2ϕ is the included angle of the equivalent axisymmetric indenter, and ζ^R is a material- and indenter-invariant constant that together with ϕ defines ξ^R.

The stress intensity factor due to the Boussinesq (normal pressure) stresses is the elastic contact SIF, K^E:

$$K^E = \chi^E \frac{P}{c^{3/2}} \ln\left(\frac{2c}{a}\right),$$ (3)

where a is the characteristic contact dimension, defined as the projected distance from the center to an impression corner. P and a are related by the hardness, $P = \alpha a^2 H$, where α is a dimensionless factor characterizing the indenter shape. a is fixed at $a_{\max}$ during unloading, again, due to the irreversibility of plastic deformation. χ^E varies with material properties according to

$$\chi^E = -\zeta^E (1 - 2\nu),$$ (4)

where ν is material Poisson's ratio and ζ^E is positive semi-empirical constant.

The wedging SIF during loading takes the form

$$K^W_{load} = \chi^W \frac{P}{c^{3/2}},$$ (5)

with an amplitude χ^W of

$$\chi^W = \zeta^W \alpha^{1/2} \frac{(\gamma^2 - 1)}{\gamma} (1 - \nu),$$ (6)

where γ is a dimensionless factor characterizing the response of the material to the wedging action of the indenter,

$$\gamma = 1 + \frac{(6 - \pi)(1 - 2\nu)}{8(1 - \nu)} \cot\phi,$$ (7)

and ζ^W is another semi-empirical constant. During the unloading half-cycle, the wedging SIF is

$$K^W_{unload} = \chi^W \frac{P}{c^{3/2}} \left(\frac{P}{P_{\max}}\right)^{(2 - \frac{3}{m})},$$ (8)

where m is the unloading exponent (see Part I). The unloading wedging SIF retains $P/c^{3/2}$ scaling only if $m = 1.5$.

The equilibrium condition $K = T$, where K is the sum of the three stress-intensity factors and T is the material toughness, provides the basis for calculation of the $c(P)$ crack length trajectories during the load-unload contact cycle. A convenient dimensionless form for this condition uses $\overline{K}$ and $\overline{T}$; the total SIF and toughness, respectively, normalized by the combined contact variable $\alpha H a_{\max}^{1/2}$. Dimensionless indentation load and radial crack length are formed accordingly as $\overline{P} = P/P_{\max}$ and $\bar{c} = c/a$, such that during loading

$$\overline{K}_{load} = \frac{\overline{P}}{\bar{c}^{3/2}} \left[\chi^R + \chi^W + \chi^E \ln(2\bar{c}/\overline{P}^{1/2})\right] = \overline{T}.$$ (9)

During unloading, the dimensionless equilibrium relationship is

$$\overline{K}_{unload} = \frac{1}{\bar{c}^{3/2}} \left[\chi^R + \chi^W \overline{P}^{(3 - 3/m)} + \chi^E \overline{P} \ln(2\bar{c})\right] = \overline{T},$$ (10)

Table 1. Mechanical properties of soda-lime glass and fused silica used in crack-evolution modeling.

Parameter	Soda-lime glass	Reference	Fused silica	Reference
T_{inert} (MPa m$^{1/2}$)	0.70	(Wiederhorn et al., 1974)	0.73	(Wiederhorn, 1969)
T_{env} (MPa m$^{1/2}$)	0.25	(Cook and Liniger, 1993)	0.34	(Sglavo and Green, 2001)
E (GPa)	70	(Anstis et al., 1981)	72	(Wiederhorn, 1969)
H (GPa)	5.7	(Morris and Cook, 2004)	7.0	(Morris and Cook, 2004)
ν	0.25	(Anstis et al., 1981)	0.18	(Wiederhorn, 1969)
m	1.45	(Morris et al., 2004)	1.25	(Morris et al., 2004)

where a remains at the fixed, maximum value a_{max} attained at peak load. Equations (9) and (10) allow for straightforward numerical determination of $\bar{c}(\overline{P})$ and thus $c(P)$ and identification of the interplay between the various SIF components as determined by their amplitude terms, χ^R, χ^W and χ^E.

3.2. Calibration of the model

Table 1 provides the mechanical properties of soda-lime glass and fused silica to be used in calibration and scaling of the amplitude parameters in the radial cracking model. We begin with the residual SIF term, χ^R, taking as our basis Vickers indentation crack lengths measured post-indentation in a silicone oil environment (Anstis et al., 1981). Under these conditions, the cracks are in inert equilibrium with the residual field, such that the relationship between the crack length, c_0, and the inert toughness, T_{inert}, gives

$$\chi^R = T_{inert}/(P/c_0^{3/2}). \tag{11}$$

The measured load-invariant indentation crack length parameters were $P/c_0^{3/2} = 13.7\,\text{MPa}\,\text{m}^{1/2}$ for soda-lime glass and $33.1\,\text{MPa}\,\text{m}^{1/2}$ for fused silica. Using these and the T_{inert} values from Table 1 in Equation (11) gives the χ^R values for Vickers indentation, 0.051 and 0.022 for soda-lime glass and fused silica, respectively. While the existence of the residual indentation stress field has been experimentally well-established for soda-lime glass (Arora et al., 1979; Marshall and Lawn, 1979; Cook and Pharr, 1990), there is much less residual stress in reaction to the deformation zone for a material that densifies substantially, such as the 'anomalous' glasses, including fused silica (Arora et al., 1979). The much-reduced value of χ^R for fused silica reflects this smaller residual stress field.

A χ^R value and known E, H and ϕ values for a given material-indenter combination in principal allow the calibration constant ζ^R to be evaluated from Equation (2) and thus χ^R to be estimated for other materials and other indenters. However, as noted above, accommodation of the indenter displacement by densification in fused silica significantly reduced the χ^R value (based on the E/H ratio and an invariant deformation pattern, fused silica should in fact have only a slightly smaller χ^R value than soda-lime glass). Similarly, a change in deformation mode with indenter acuity prevents simple extrapolation in ϕ. Figure 1 is a series of SEM images of 200 mN
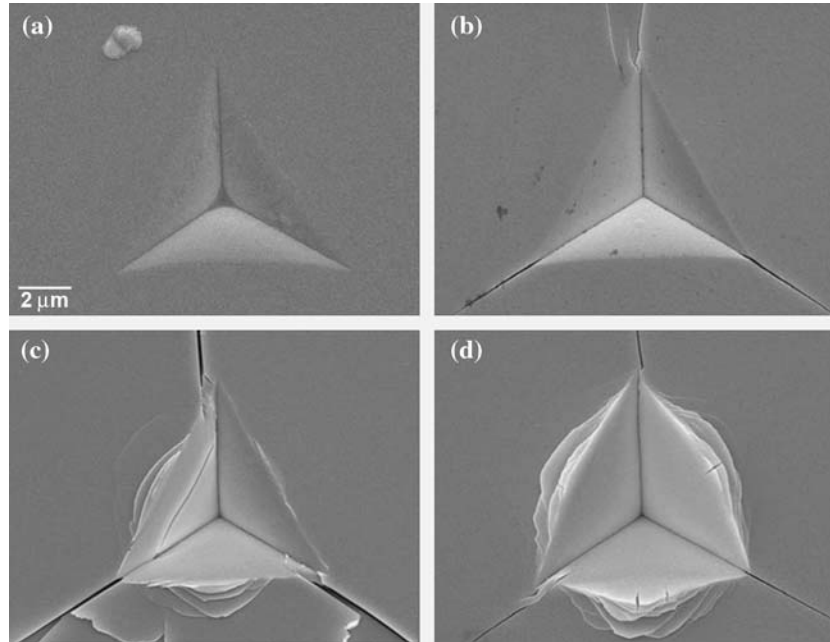
Figure 1. Scanning-electron images of residual impressions of 200 mN indentations on soda-lime glass by (a) Berkovich ($\phi = 70.3°$), (b) $\phi = 58.9°$ (c) $\phi = 49.6°$ (d) cube-corner ($\phi = 42.3°$). Plasticity is contained at Berkovich and $\phi = 58.9°$ indentations, and uncontained at the $\phi = 49.6°$ and cube-corner indentations.

peak-load indentations on soda-lime glass performed with sharp pyramids varying in acuity from the Berkovich ($\phi = 70.3°$) to the cube-corner ($\phi = 42.3°$). There is a transition from fully-contained plasticity to unconstrained plasticity ('pile-up' of plastically deformed material around the indenter) somewhere between $\phi = 58.9°$ and $\phi = 49.6°$ for indentations on soda-lime glass. Pile-up reduces the constraint of the surrounding elastic matrix on the plastic deformation zone, and necessarily reduces the strength of the residual stress field, setting an upper limit on the value of χ^R that can be achieved for a particular material (Lawn et al., 1980). Using the Vickers indenter χ^R values above and the E and H values from Table 1 in Equation (2), the indenter invariant ζ^R parameters for soda-lime glass and fused silica are 0.0289 and 0.0136, respectively. Using these to scale χ^R to the pile-up transition range via the angular dependence of Equation (2) gives upper bound estimates of χ^R for the two materials as 0.082 for soda-lime glass and 0.035 for fused silica. Figure 2 shows contours of χ^R using Equation (2) and soda-lime glass as a basis, illustrating the dependence on E/H and ϕ and the extrapolation of χ^R from the Vickers indentation measurement to the unconstrained plasticity limit. Fused silica exhibits similar behavior with the contours depressed by about 60% and the symbols shifted to slightly smaller E/H values. χ^R values are listed in Table 2. In both materials, but particularly fused silica, the χ^R values appropriate to the cube-corner probe are substantially smaller than $\chi^R = 0.14$ computed using $\xi^R = 0.040$ (Pharr, 1998) as estimated from *post-situ* crack length measurements.

The wedging and elastic-contact SIF terms, χ^W and χ^E can be calibrated from *in-situ* fracture data, and we take as a basis cube-corner soda-lime glass fracture
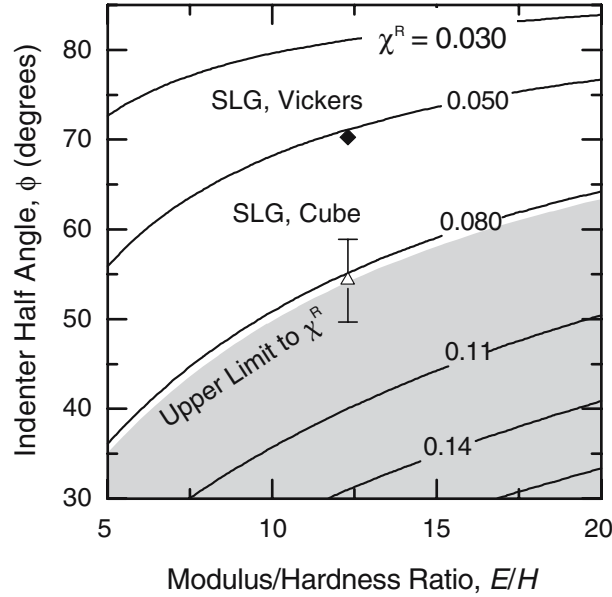
Figure 2. (a) Map of χ^R as a function of ϕ and E/H, calculated with Equation (2) for soda-lime glass, calibrated via Vickers indentation (solid symbol). The value for cube-corner indentation was extrapolated to the unconstrained plasticity limit (open symbol).

evolution measured in silicone oil (Morris and Cook, 2004) (recapitulated as Figure 1(a) in Part I). The three-field crack evolution model shows that, during loading, Equation (9), the effective crack-driving force amplitude is the sum $\left(\chi^R + \chi^W\right)$. Therefore, the crack evolution data may be re-interpreted as following a trajectory of slope $\chi^E/\left(\chi^R + \chi^W\right) = -0.50$ and intercept $T/\left(\chi^R + \chi^W\right) = 0.48\,\text{MPa m}^{1/2}$. Together with the inert-environment toughness (Table 1), the total crack-driving force amplitude is $\chi^R + \chi^W = 1.46$, and the elastic-contact amplitude is $\chi^E = -0.73$. Using $\chi^R = 0.08$ (Table 2) appropriate to cube-corner indentation of soda-lime glass gives the wedging amplitude as $\chi^W = 1.38$. The physics of acute indentation fracture is made clear in comparison of the amplitude terms as they appear in Equations (9) and (10): crack evolution is determined by the transient competition between the wedging and elastic-contact fields, with the residual plastic deformation field a weak perturbation.

Scaling of the wedging term χ^W is dominated by the factor γ, which corrects the indentation field for the transverse displacements omitted in determining the contact stiffness of obtuse probes. Figure 3(a) is a contour map of γ as a function of ϕ and ν using Equation (7); the locations of cube-corner and Vickers indentations on soda-lime glass and fused silica are indicated (ν values from Table 1). The effects of increased probe acuity (measured by $\cot \phi$) to increase γ and, to a lesser extent, increased coupling of transverse and axial displacements (measured by ν) to decrease γ are obvious. Expanding the scaling relation for χ^W, Equation (6), about the experimental point for soda-lime glass cube-corner indentation using $\zeta^W = 3.44$ and these γ values gives the χ^W values for other materials and indenters. Figure 3(b) is a contour plot of χ^W as a function of of ϕ and ν for three-sided pyramids, $\alpha = 3^{3/2}/4 \cong 1.30$. The experimental calibration point is shown as the solid symbol and the extrapolated points are shown as the open symbols. (The Vickers indenter points do not lie exactly
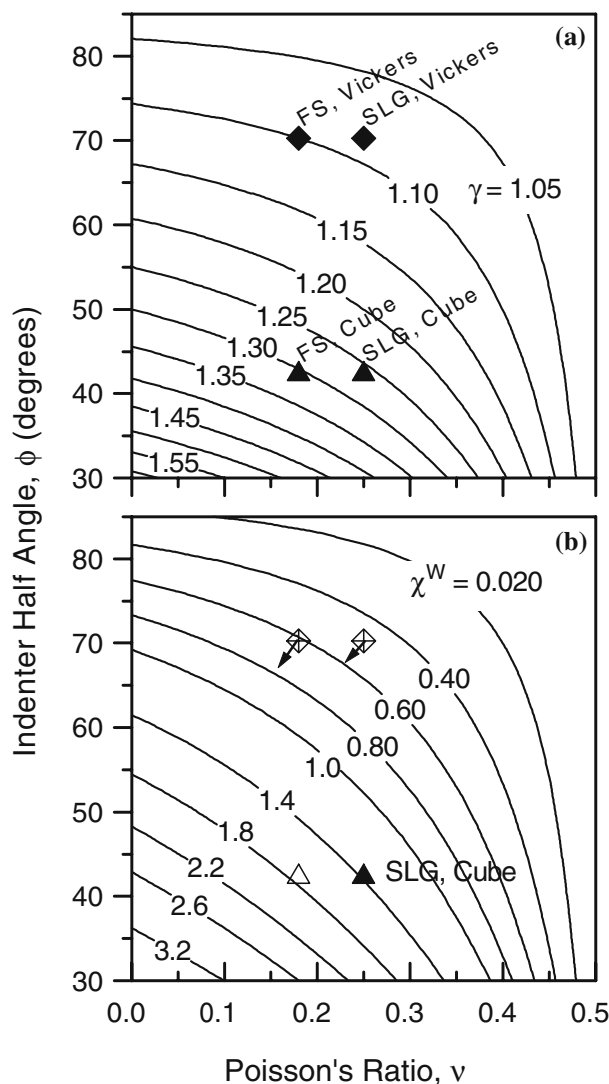
Figure 3. (a) Map of γ as a function of ϕ and ν, calculated with Equation (7). (b) Map of χ^{W} as a function of ϕ and ν, calculated with Equation (6) for cube-corner indentation, calibrated via soda-lime glass measurements (solid symbol). The values for fused silica and Vickers indentation were extrapolated via ϕ and ν as shown (open symbols).

on the contours indicated as $\alpha = 2$ for four-sided pyramids. The arrows indicate the approximate correct positions.) χ^{W} values are listed in Table 2.

The scaling of the elastic-contact term χ^{E} is straightforward from Equation (4); the experimental point for soda-lime glass cube-corner indentation gives $\zeta^{E} = 1.46$ from which the linear extrapolation in ν to obtain the fused silica value is shown in Figure 4. As observed in Equation (4), within the context of the three-field model these values are indenter acuity invariant. Comparison may be made with previous obtuse indenter observations, however, for which a good approximation is a two-field description: the elastic + wedging components are combined into a single reversible component with functional crack length dependence given by Equation (3) and a

Table 2. Indentation parameters for fracture evolution modeling.

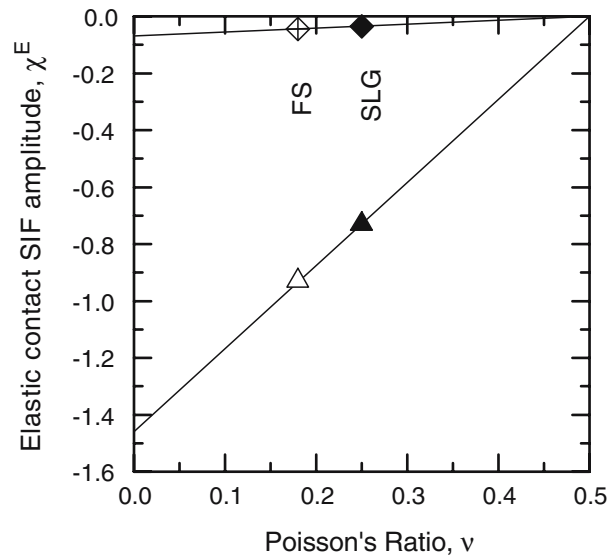| Material	Indenter / Model	α	χ^R	χ^W	χ^E
Soda-lime glass	Vickers / 2-field	2	0.051	0	−0.035
	Vickers / 3-field	2	0.051	0.60	−0.73
	Cube-corner / 2-field	1.3	0.082	0	−0.035
	Cube-corner / 3-field	1.3	0.082	1.38	−0.73
Fused silica	Vickers / 2-field	2	0.022	0	−0.045
	Vickers / 3-field	2	0.022	0.76	−0.93
	Cube-corner / 3-field	1.3	0.035	1.38	−0.93

Figure 4. Plot of χ^E as a function of ν for three-field indentation model (lower line) and two-field model (upper line), calibrated via soda-lime glass measurements (solid symbols). The values for fused silica were extrapolated via ν (open symbols).

reduced amplitude term that reflects the competition between the underlying components. Analysis in this way of radial crack growth at Vickers indentations in soda-lime glass gives the reduced two-field calibration factor $\zeta^E = 0.07$ (Lawn et al., 1980; Morris and Cook, 2004). The experimental point and extrapolation for fused silica value in this context are also shown in Figure 4. The physics of obtuse indentation fracture is made clear by comparison of this effective amplitude term with the residual term: crack evolution is determined by the competition between an effective reversible field and the irreversible residual field. χ^E values are listed in Table 2.

3.3. Crack evolution during the indentation cycle

Figure 5(a) is a plot of crack evolution in soda-lime glass, measured *in situ* during cube-corner indentation in an inert environment (silicone oil). The two- and three-field fracture predictions are shown as the dashed and solid lines, respectively, using Equations (9) and (10), the peak loads indicated and the parameters listed in
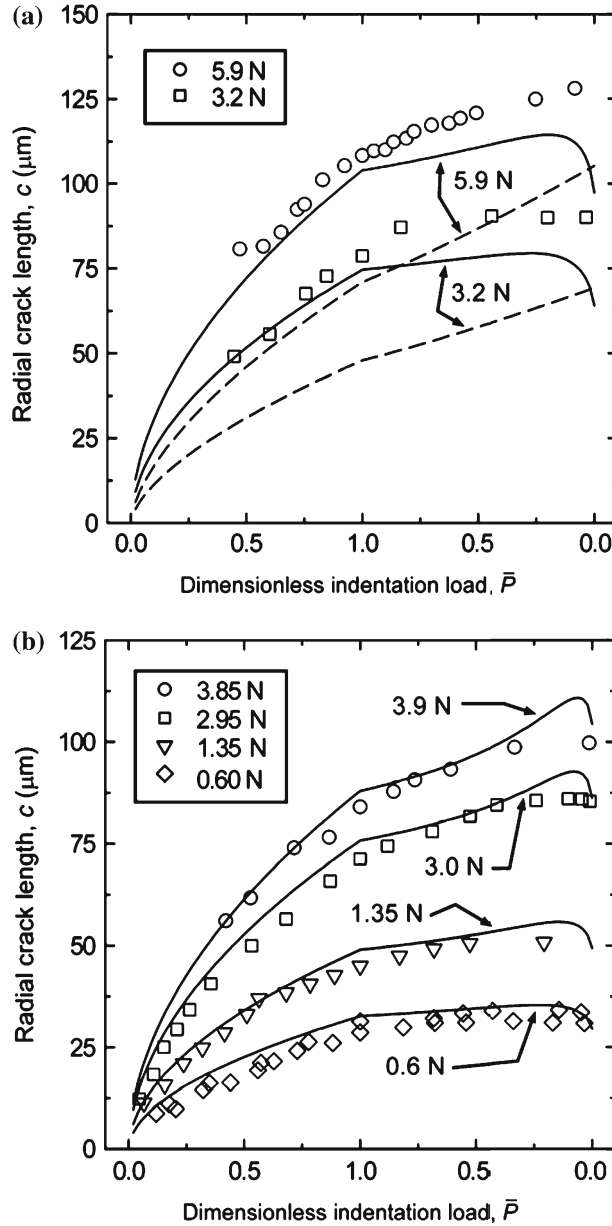
Figure 5. In-situ radial crack data for cube-corner indentation of soda-lime glass: (a) compared with the three-field and two-field models in silicone oil; (b) compared with the three-field model in ambient air.

Tables 1 and 2. While the three-field model does not reproduce the experimental data exactly, the features of radial crack evolution for cube-corners are certainly captured: Radial crack growth dominates the loading half-cycle, and there is little radial crack growth on unloading. The two-field model underestimates the crack lengths throughout the contact cycle and predicts an increasing crack length during unloading that is not observed. Figure 5(b) is a similar series of plots of *in-situ* fracture data for soda-lime glass in a reactive environment (ambient air). Appropriate to the fracture
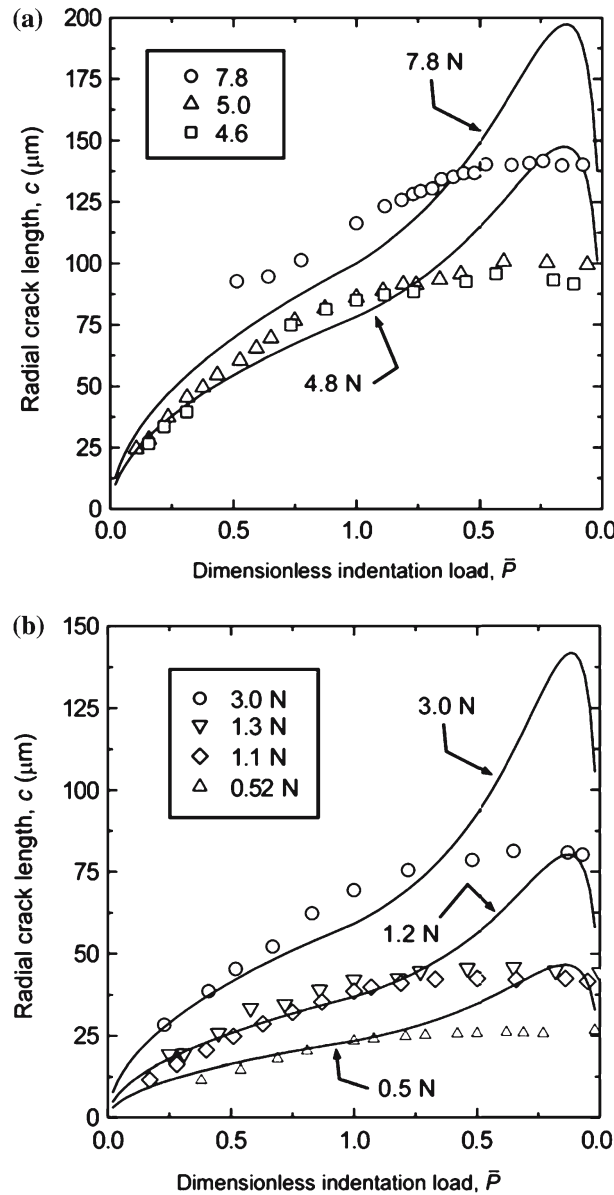
Figure 6. In-situ radial crack data for cube-corner indentation on fused silica: (a) compared with the three-field model in silicone oil; (b) compared with the three-field model in ambient air.

environment, the toughness of the glass was set to the smaller value, T_{env}, (Table 1) in making the three-field crack evolution predictions. The three-field model describes the radial crack-length evolution very well, except perhaps in the final stages of unloading.

Three-field crack evolution model predictions are compared with *in-situ* radial crack measurements for cube-corner indentation of fused silica in silicone oil and ambient air in Figures 6(a) and (b), respectively (using appropriate material parameters as per Tables 1 and 2). For both environments, the crack-length response is adequately represented during the loading portion of the contact. However, the wedging
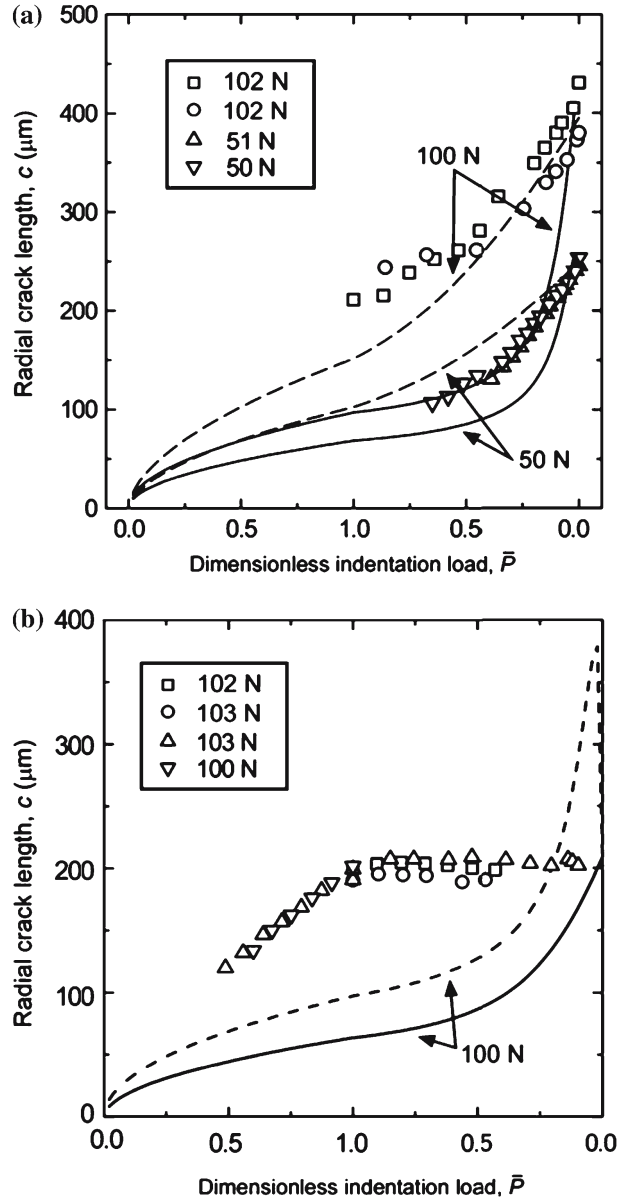
Figure 7. In-situ radial crack data for Vickers indentation in ambient air compared with the three-field and two-field models: (a) soda-lime glass; (b) fused silica.

model does not represent the crack-length response very well during unloading—in each case, the model predictions are marked by a large peak in crack length near complete unload that is not observed experimentally.

Figure 7 is a series of comparisons of crack evolution trajectories during Vickers indentation of (a) soda-lime glass and (b) fused silica in silicone oil. Two- and three-field fracture predictions are shown as the dashed and solid lines, respectively; for both materials the indentation loads are much greater than those used during cube-corner indentation. For soda-lime glass, the two-field model in this case does a much better job of describing the observations, particularly the increase in crack length

during unloading—a result that is not too surprising given that Vickers-soda-lime glass observations such as these motivated the development of the two-field model in the first place (Marshall and Lawn, 1979). The three-field model underestimates the radial crack lengths by a great deal until almost complete unload. For fused silica, both predictions are inadequate except at the conclusion of the cycle, where the (calibrated) residual SIF provides agreement with the crack lengths.

3.4. METASTABLE RADIAL CRACK TRAPPING

The previous section showed that the wedging crack evolution model is able to describe crack evolution in both soda-lime glass and fused silica, if there is perhaps some deficiency in the description of unloading in the final stages. In particular, the net SIF and thus equilibrium crack length passes through a maximum during the final stages of the unloading cycle (Figures 5–7 and Figure 14 in Part I). If cracks cannot heal, then the crack length at full unload (observed after the contact event) may be metastably trapped in a sub-equilibrium configuration. It is therefore desirable to find the maximum crack length in the unloading cycle. Equation (10) may be differentiated with respect to $\overline{P}$, and solved for the load at maximum $\overline{K}$ and constant $\bar{c}$:

$$\overline{P}\left(\overline{T}\right)\big|_{\bar{c}} = \left(-\frac{\chi^E \ln\left(2\bar{c}\right)}{3\chi^W}\frac{m}{m-1}\right)^{\frac{m}{2m-3}} \tag{12}$$

Equation (12) is an expression for the dimensionless indentation load at which an equilibrium crack will reach a maximum. Furthermore, this expression predicts that the existence of metastable trapping phenomena depends, from a material-probe geometry point of view, only on the χ^W/χ^E ratio and the unloading exponent m.

   Substitution of Equation (12) back into Equation (10) forms the dimensionless SIF level for metastably trapped cracks, $\overline{K}_{\mathrm{meta}}$:

$$\overline{K}_{\mathrm{meta}} = \chi^R \frac{1}{\bar{c}^{3/2}} + \Delta\overline{K} \tag{13}$$

where $\Delta\overline{K}$ is a dimensionless increment of metastable trapping, and is equal to

$$\Delta\overline{K} = (\chi^W B + \chi^E B^{m/(3m-3)})\frac{[\ln(2\bar{c})]^{(3m-3)/(2m-3)}}{\bar{c}^{3/2}} \tag{14}$$

with

$$B = \left(-\frac{\chi^E}{\chi^W}\frac{m}{(3m-3)}\right)^{(3m-3)/(2m-3)}. \tag{15}$$

   Inspection of Equations (14) and (15) shows that the result of the conventional (residual-stress only) model is recovered as $\chi^W \to 0$ only for $1 < m < 1.5$, and therefore these limits define the physically admissible range of m (within the model). Figure 8 is a plot of $\overline{K}$ vs. $\bar{c}$ for cube-corner indentation on soda-lime glass (which may be compared with Figure 13 in Part I) with the peak load $\overline{P} = 1$ line, the unload $\overline{P} = 0$ (equilibrium with the residual field only) line, and the maximum crack
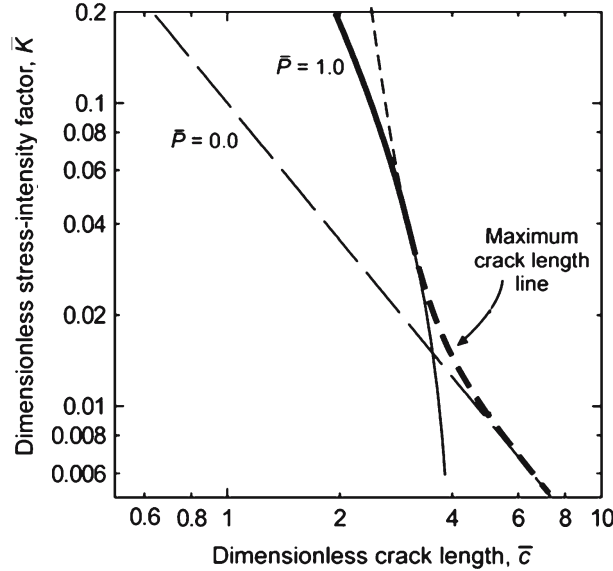
Figure 8. Metastable trapping in dimensionless coordinates, with the maximum crack length line of Equation (13). The bold line is the full metastable cracking relationship, which connects the maximum crack length line (short-dash) at large $\bar{c}$ to the $\overline{P}=1$ (solid) line for smaller $\bar{c}$. At large $\bar{c}$, the maximum crack length line approaches the $\overline{P}=0$ (long-dash) residual-field-only line.

length line of Equation (13). The maximum crack length response coincides with the $\overline{P}=1$ response at $\bar{c}=(1/2)\exp[3(1-m)\chi^W/m\chi^E]$, and asymptotically approaches the $\overline{P}=0$ response at large $\bar{c}$. The complete metastable response, shown as the bold line, is formed by connecting the $\overline{P}=1$ line for crack lengths less than the coincident point to the maximum crack length line.

Using Equation (12), the point of maximum crack length during the unloading half-cycle may be mapped onto a plot of $\overline{P}$ vs. $\bar{c}$ as a function of the χ^W/χ^E ratio with fixed m. Although $-\chi^W/\chi^E$ is approximately invariant with material properties (see Discussion), the point in the unloading cycle at which crack-length maxima are reached is a strong function of m. Fused silica ($m \approx 1.25$) and soda-lime glass ($m \approx 1.45$) nearly span the range of experimentally observed m at sharp contacts, (Oliver and Pharr, 1992; Pharr and Bolshakov, 2002, Morris et al., 2004) and this allows for some possible experimental distinction between the two glasses.

Figure 9(a) is a map of maximum crack length-load loci in the unloading cycle as a function of $-\chi^W/\chi^E$ for $m = 1.45$, appropriate for soda-lime glass (Table 1). Superimposed on the figure are estimates of $\overline{P}$ at maximum $\bar{c}$ from *in-situ* cube-corner indentation observations on soda-lime glass; the symbols represent the maximum estimated crack length and associated load point and the load range for adjacent observations. While the uncertainty in $\overline{P}$ is significant, the data group about the $-\chi^W/\chi^E = 2.0$ line, consistent with $-\chi^W/\chi^E$ as estimated from the loading half-cycle (Figure (4) and Table 2). It is noted for Vickers indentation, with $-\chi^W/\chi^E = 0.7$, the maximum crack length is at complete unload over all practical range of $\bar{c}$, in agreement with experiment (e.g., Figure 7).

Figure 9(b) is a similar map of $-\chi^W/\chi^E$ for $m = 1.25$, appropriate to fused silica. Immediately obvious is the decrease in sensitivity of the contours on $\bar{c}$ compared
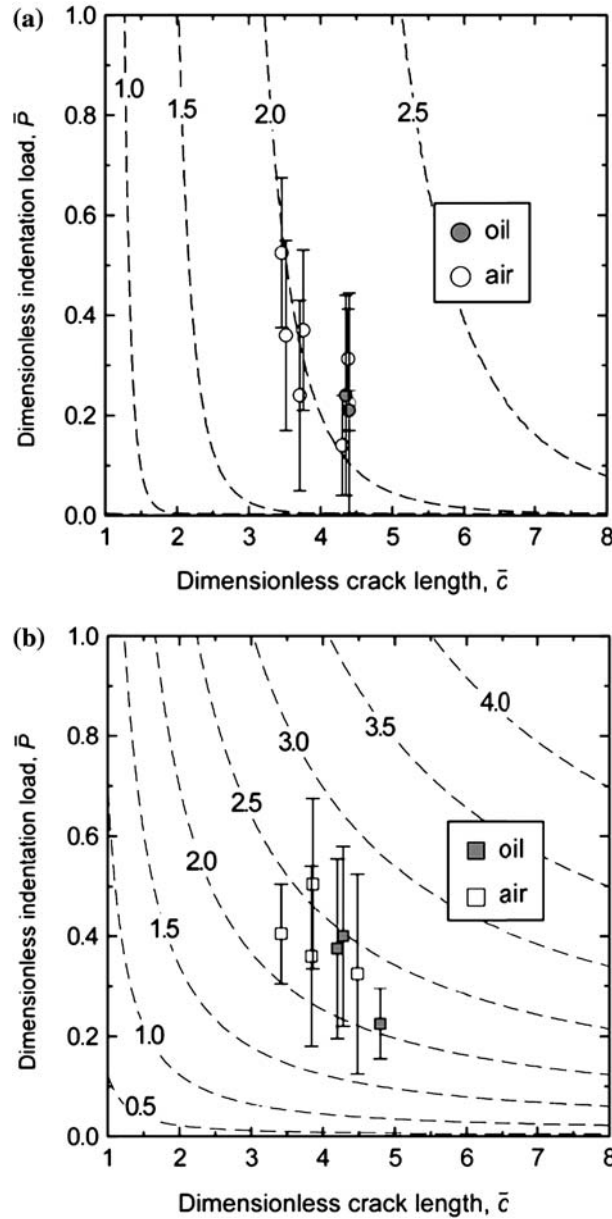
Figure 9. Maps of the point in the unloading cycle at which crack length reaches a maximum for (a) soda-lime glass and (b) fused silica. Superimposed on both maps are experimental observations of crack length maxima for experiments in silicone oil and ambient air.

to the $m = 1.45$ case. Again, estimates of $\overline{P}$ at maximum $\bar{c}$ from *in-situ* cube-corner indentation observations on fused silica are superimposed, estimated in the same way as for soda-lime glass. The experimental data mainly lie in the band $2.0 < -\chi^{W}/\chi^{E} < 2.5$, and appear to follow the same trend as the lines of constant χ^{W}/χ^{E}. While the model greatly overestimates the maximum crack length for fused silica in the later stages of unloading (Figure 6), there appears to be some success in predicting the point in the indentation cycle of maximum crack length.

4. Discussion

4.1. WEDGING PHENOMENA AND STRESS-FIELD SCALING

The experimental observations here suggest that a reversible, tensile, plastic-deformation mechanism-insensitive stress field drives fracture during acute indentation. While the evidence for this 'wedging' field is by no means exhaustive at this point, the *in-situ* fracture experiments exhibiting very high driving forces during loading, failure of the two-field crack evolution model and successful scaling of the wedging field by indenter angle and material Poisson's ratio, along with supporting observations of indenter acuity-related fracture phenomena during instrumented indentation, are all compelling evidence. Of course, reversible, elastic indentation stress fields causing fracture is not new—the ring and cone cracking system common for Hertzian contacts is the most well-known example (Frank and Lawn, 1967, Cook and Pharr, 1990).

An important assumption in developing the wedging field was representation of the lateral contact displacements as a surface-located blister field, with the accompanying $\sigma \sim 1/r^3$ stress dependence. The experimental basis for this assumption is the *in-situ* experiments that show an apparent SIF of type $P/c^{3/2}$, which corresponds to a $\sigma \sim 1/r^3$ field, and another of type $P/c^{3/2} \ln(2c/a)$, corresponding to the $\sigma \sim 1/r^2$ field attributed to the Boussinesq field (Lawn et al., 1980). It is possible that this result is a consequence of presumptively choosing the forms of the stress fields prior to plotting experimental data (that is, there was no attempt to characterize the data as resulting from, say, $\sigma \sim 1/r$ or $\sigma \sim 1/r^4$ fields). However, as Yoffe has shown (Yoffe, 1986), the stress field arising from an axisymmetric surface *shear* distribution over a contact of radius a is equivalent to the blister field in the far field, $r \gg a$. In retrospect, then, it is not surprising that imposed lateral displacements (presumably resulting in significant shear) at a contact would manifest themselves as the blister-field-like wedging phenomena explored in this work.

Another assumption used in constructing the form of the wedging field was that axial and lateral displacements within the contact zone were independent. This assumption is not a conservative one—displacements are certainly not independent—and imposed lateral vs. axial displacements beneath the contacted surface are competing effects for any $\nu > 0$. It may be that one of the primary manifestations of lateral displacement at the contact is a wide gap between the net resisting force amplitude ($\chi^E + \chi^W = -0.12$) measured for cube-corner and the value ($\chi^E = -0.035$) measured for Vickers fracture on soda-lime glass (Figures 3 and 4). A possible reason for this discrepancy is crack shape: Cube-corner radial cracks were noted to definitely intersect the surface along their entire length (Morris and Cook, 2004), while Vickers radial cracks are observed to exist largely subsurface during most of the indentation cycle, where they are shielded from the highest compressive stresses of the Boussinesq field (Cook and Pharr, 1990; Tandon et al., 1990). Another explanation is that the Boussinesq field is not a good approximation at intermediate distances for the contact stress field of a very acute indenter, in that the wedging and contact stress fields interact significantly in this range. This is a subject for future theoretical and experimental study.

The relative importance of the wedging field for a given indenter may be assessed by the ratio $-\chi^W/\chi^E$. Expanding this ratio using Equations 4, 6 and 7, using

$\gamma - 1 \gg 1$ (see Figure 2(a), this is a good approximation for most indenter-material combinations), gives $-\chi^W/\chi^E \approx 3\zeta^W \alpha^{1/2} \cot\phi/4\zeta^E$; a parameter invariant with respect to material Poisson's ratio and sensitive only to the probe acuity, ϕ, at least when ϕ is large. With this observation, $-\chi^W/\chi^E$ may be interpreted as a rough measure of the 'wedginess'—the relative flat-punch-to-needle-like behavior—of a particular probe geometry.

4.2. Wedging fracture evolution model

If a wedging phenomenon is, in fact, an important or even dominant mechanism for very acute probes, this complicates the interpretation of post-indentation fracture results. Still, there are possible ways in which to exploit wedging phenomena. First among them is the estimation of the fracture toughness of materials that have a great deal of porosity, or free volume, where the elastic-plastic model would surely fail due to accommodation of permanent deformation by compaction (Cook et al., 2004). We consider here the practical implications of the wedging fracture evolution description for post-indentation behavior and in the final stages of unloading.

For conventional materials evaluation, the greatest implication of the wedging fracture evolution model is that, with the possibility of metastable crack trapping, there will be deviation from the $c \sim P^{2/3}$ scaling predicted for a residual-field only radial-crack configuration. From the three published calibrations of ξ^R for cube-corner indenters (Pharr et al., 1993; Harding et al., 1995; Pharr, 1998), it appears that after the indentation event the $c \sim P^{2/3}$ scaling is approximately obeyed. Examination of Figure 8, however, shows that metastable trapping is most important for the smallest indentation loads (greater $\overline{K}$), exactly where experimentation is most difficult: The μm and sub-μm cracks produced at the very smallest ('nano'-)indentation loads will be affected by surface forces on a length scale not normally important for the macroscopic cracks produced by conventional (Vickers) indentation fracture, especially if there is insufficient residual stress to hold the cracks open. Crack closure nearest the crack tip makes detection of the tip of the crack especially difficult in imaging methods that are mostly sensitive to topography, such as secondary-electron or scanning-probe microscopy. The purpose of this discussion is not to dismiss previous experimental results, but to acknowledge that there are still considerable experimental difficulties when studying fracture at very small length scales.

Another phenomenon that may affect the perceived c vs. P relationship is post-indentation radial crack pop-in. All of the preceding discussion has been predicated on the existence of a stable radial crack, existing primarily outside of the contacted area, throughout the entire indentation cycle. If crack initiation happens after the indentation event, then the radial cracks will grow to a final length in the presence of the residual field only. A full indentation fracture response for a material that has a significant residual field and is susceptible to slow crack growth, such as soda-lime glass and many other oxide ceramics, might be imagined thusly: no radial cracking at the smallest loads; post-indentation radial fracture with attendant equilibrium $c \sim P^{2/3}$ scaling at larger loads; an abrupt jump in crack length as cracks are initiated during the indentation cycle and are metastably trapped at still larger peak indentation loads; and then eventual recovery of $c \sim P^{2/3}$ scaling at the greatest loads as the Boussinesq-like stresses squelch the effects of wedging.

A quantity of possible experimental interest is $\Delta \overline{K}$, the stress-intensity factor difference between a radial crack at equilibrium size and at the maximum crack length in the presence of the residual stress field. $\Delta \overline{K}$ is therefore a measure of the amount of metastable trapping of radial cracks after complete unload, a practical quantity that would be required in estimating the stress level needed to repropagate indentation flaws after their introduction onto a material surface, or, the reduction in toughness (as, for example, when suddenly exposed to a corrosive environment) needed to repropagate indentation flaws under the influence of the residual field only. From a modeling point of view, the greatest deficiency in the wedging indentation model is prediction of crack size during the unloading half-cycle, especially for the later stages of unloading and low-m materials, such as fused silica. By Equation 10, K^W persists later in the unloading half-cycle than K^E, and persistence is strengthened by smaller m, which gives rise to the great amount of crack growth in the last half of the unloading half-cycle, Figure 6. So while quantification of $\Delta \overline{K}$ is desirable for many reasons, including those above, the model in this article is likely to overestimate $\Delta \overline{K}$. However, the *in-situ* fracture data show that cracks reach maximum size well before complete unload, indicating that the phenomenon of metastable trapping of radial cracks should be included in practical consideration of acute contacts.

Finally, it has been demonstrated that the unloading of a sharp indenter from a residual impression of an elastic-plastic indentation is analogous to the unloading of a 'power-law' indenter with a shape described by $z = Fr^{\frac{1}{m-1}}$ (Pharr and Bolshakov, 2002) (where F is some constant). The implication is that the acuity of the indenter effectively decreases with unloading, until at very small contact radii (relative to the residual impression) the contact is well described by Hertzian mechanics. At this stage, the wedging stresses would become very small compared to the Boussinesq-like stresses arising from normal pressure. The consequence for this work is that our approximation of the unloading stress (and fracture) fields is likely to be good in the initial stages of unloading, but expected to break down during the final stages of unloading, exactly as observed in Figures 5 and 6. Considering that the current unloading crack-length model accepts no further inputs, save the independently-determined unloading exponent m, the agreement is satisfactory. This points the way for further improvement of the indentation wedging model of Part I.

It was also noted that the only acceptable range for m (found by testing for recovery of the residual-stress model, Equations 13–15, as $\chi^W \rightarrow 0$) was for $1 < m < 1.5$. This is an interesting result. The Sneddon solution for axisymmetric indentation shows that $m = 1$ for a flat punch, $m = 2$ for a geometrically similar (conical) punch, and $m = 1.5$ for indentation by a parabola of revolution; forming the generally accepted range for elastic unloading at an elastic-plastic indentation, $1 \leq m \leq 2$ (Pharr and Bolshakov, 2002). Most published values for m are in the range 1.25–1.50 (Pharr and Bolshakov, 2002; Morris et al., 2004), in the acceptable range of the wedging crack evolution model. Recent finite-element work shows that there is a definite physical basis for $m \cong 1.5$— a consequence of the smoothing of the pressure distribution under the contact as a result of plastic deformation (leading to the equivalent power-law indenter described above of form $z = Fr^2$). However, the obvious problem with the wedging formulation is the failure of K^W_{unload} for a perfectly elastic indentation cycle for a sharp probe, when m must equal 2. This is a consequence of choosing the inner boundary of the crack

as $a_{\max}$ when forming K^W_{unload}. If the instantaneous contact boundary during unloading, a', (Equation 20, Part I) is substituted for $a_{\max}$ as a lower limit when forming the wedging SIF by integration, then K^W_{unload} becomes

$$K^W_{\text{unload}} = \chi^W \frac{P}{c^{3/2}} \left(\frac{P}{P_{\max}} \right)^{\left(1 - \frac{2}{m}\right)} . \tag{16}$$

Duplication of the development of Section 3.4 with Equation (16) shows that the residual-stress only model is recovered for $1 < m < 2$ with the above expression for K^W_{unload}. As a practical matter, choosing $a_{\max}$ as the inner crack boundary is physically justified at least as well as choosing a' for any material that exhibits irreversible deformation. The K^W_{unload} of Equation (16) may be a better SIF than Equation (8) for materials that fully recover within the contact zone from sharp indentation, such as rubbers and elastomers.

5. Summary

Crack growth measured during the loading half-cycle of cube-corner indentation on soda-lime glass was used here to calibrate the amplitudes of the dominant and competing wedging and elastic-contact crack-driving and -resisting forces in a three-field fracture model. Crack lengths measured after complete unload of Vickers indentation on soda-lime glass were used to calibrate the small, perturbing residual stress field amplitude; observations of indentations by probes of varying acuity indicated an upper bound to this amplitude set by unconstrained plastic deformation at very acute indentations. Elastic and plastic material properties were used to scale these amplitude terms to values applicable to fused silica indentation and indenter effective included angle was used to scale the amplitude terms to values applicable to Vickers indentation. Direct comparison of crack lengths measured *in situ* during cube-corner indentation with scaled predictions of the three-field model for a range of indentation loads revealed very good agreement during the loading half-cycle and initial stages unloading for both soda-lime glass and fused silica. A characteristic of the observations and predictions is substantial crack growth on loading and very little growth on unloading. A feature of the model, in fact, is that a metastably-trapped maximum crack length is predicted at an intermediate stage of unloading. Measurement of the relative dimensions and position in the unloading half-cycle at which these maxima were observed were in agreement with the loading-cycle based calibration of the wedging to elastic contact field amplitude ratios (although absolute crack lengths were somewhat over predicted). Whilst material and indentation-load scaling were relative successful, indenter acuity scaling to from cube-corner to the relatively obtuse Vickers indenter was less so; a previous two-field model predicted the observed crack extension during unloading from relatively large load Vickers indentation on soda-lime glass, whereas the three-field model significantly under-predicted crack extension throughout the cycle. Both two- and three-field models were inadequate for Vickers indentation of fused silica, although, as for the cube-corner, the three-field model captured the observed crack growth on loading and stagnation on unloading.

For most practical indenter geometries, the ratio of crack-driving to crack-resisting amplitudes within the context of the model, χ^W / χ^E, is approximately independent

of material properties for fixed indenter geometry, suggesting that there is a material-independent measure of 'wedginess' for a particular probe that dictates crack development during indentation. Quantitative predictions of crack development, both throughout an indentation cycle and at specific points in the cycle, can be made to test the validity of the model as a function of wedginess, as was performed here. In particular, while existing evidence seems to support the wedging hypothesis, more *in-situ* work should be performed to explore the scaling properties with probes of varying acuity: increasing wedginess should drive greater crack growth earlier in the contact cycle independent of material. Conversely, *in-situ* work with a probe of fixed wedginess should exhibit invariant crack development as materials are varied, although experimentally varying Poisson's ratio or the modulus/hardness ratio over a wide range is more difficult, especially with transparent, ideally brittle materials.

References

Anstis,G.R., Chantikul, P., Lawn, B.R. and Marshall, D.B. (1981). A critical evaluation of indentation techniques for measuring fracture toughness. I. Direct crack measurements. *Journal of the American Ceramic Society* **64**, 533–538.

Arora,A., Marshall, D.B., Lawn, B.R. and Swain, M.V. (1979). Indentation deformation/fracture of normal and anomalous glasses. *Journal of Non-Crystalline Solids* **31**, 415–428.

Cook, R.F. and Liniger, E.G. (1993). Kinetics of indentation cracking in glass. *Journal of the American Ceramic Society* **76**, 1096–1105.

Cook, R.F. and Pharr, G.M. (1990). Direct observation and analysis of indentation cracking in glasses and ceramics. *Journal of the American Ceramic Society* **73**, 787–817.

Cook, R.F., Morris, D.J. and Thurn, J. (2004). Toughness and contact behavior of conventional and low-k dielectric thin films. In: *Thin Films – Stresses and Mechanical Properties X.* Edited by Corcoran, S.G., Joo, Y.-C., Moody, N.R. and Suo, Z. Materials Research Society, Warrendale, PA pp. U4.1.1–12.

Frank, F.C. and Lawn, B.R. (1967). On the Theory of Hertzian Fracture. *Proceedings of the Royal Society of London Series A*, **A229**, 291–306.

Harding, D.S., Oliver, W.C. and Pharr, G.M. (1995). Cracking during nanoindentation and its use in the measurement of fracture toughness. In: *Thin Films – Stresses and Mechanical Properties V.* (Edited by Baker, S.P., Ross, C.A., Townsend, P.H., Volkert, C.A. and Borgesen, P.) Materials Research Society, Warrendale, PA, pp. 663–668.

Lawn, B.R., Evans, A.G. and Marshall, D.B. (1980). Elastic/plastic indentation damage in ceramics: The median/radial crack system. *Journal of the American Ceramic Society* **63**, 574–581.

Marshall, D.B. and Lawn, B.R. (1979). Residual stress effects in sharp contact cracking I. Indentation fracture mechanics. *Journal of Materials Science* **14**, 2001–2012.

Morris, D.J. and Cook, R.F. Radial fracture during indentation by acute probes: I, Description by an indentation wedging model. *International Journal of Fracture* (submitted).

Morris, D.J. and Cook, R.F. (2004). In situ cube-corner indentation of soda-lime glass and fused silica. *Journal of the American Ceramic Society* **87**, 1494–1501.

Morris, D.J., Myers, S.B. and Cook, R.F. (2004). Sharp probes of varying acuity: Instrumented indentation and fracture behavior. *Journal of Materials Research* **19**, 165–175.

Oliver, W.C. and Pharr, G.M. (1992). An improved technique for determining hardness and elastic modulus using load and displacement sensing indentation experiments. *Journal of Materials Research* **7**, 1564–1583.

Pharr, G.M. (1998). Measurement of mechanical properties by ultra-low load indentation. *Materials Science & Engineering A* **A253**, 151–159.

Pharr, G.M. and Bolshakov, A. (2002). Understanding nanoindentation unloading curves. *Journal of Materials Research* **17**, 2660–2671.

Pharr, G.M., Harding, D.S. and Oliver, W.C. (1993). Measurement of fracture toughness in thin films and small volumes using nanoindentation methods. In: *Mechanical Properties and Deformation Behavior of Materials Having Ultra-Fine Microstructures.* (Edited by Nastasi, M., Parkin, D.M. and Gleiter, H.) NATO ASI, Boston, MA, pp. 449–461.

Sglavo, V.M. and Green, D.J. (2001). Fatigue limit in fused silica. *Journal of the European Ceramic Society* **21**, 561–567.

Tandon, R., Green, D.J. and Cook, R.F. (1990). Surface stress effects on indentation fracture sequences. *Journal of the American Ceramic Society* **73**, 2619–2127.

Wiederhorn, S.M. (1969). Fracture surface energy of glass. *Journal of the American Ceramic Society* **52**, 99–105.

Wiederhorn, S.M., Johnson, H., Diness, A.M. and Heuer, A.H. (1974). Fracture of glass in vacuum. *American Ceramic Society Bulletin* **52**, 336–341.

Yoffe, E. H. (1986). Stress fields of radial shear tractions applied to an elastic half-space. *Philosophical Magazine A: Physics of Condensed Matter, Defects and Mechanical Properties* **54**, 115–129.